Acta Materialia 259 (2023) 119282

Contents lists available at ScienceDirect

Acta Materialia

journal homepage: www.elsevier.com/locate/actamat

Full length article

A combined DFT and NPD approach to determine the structure and composition of the ε-phase of tungsten boride

S.S. Setayandeh [a,*], J.H. Stansby [a], E.G. Obbard [a], M.I. Brand [a], D.M. Miskovic [b], K.J. Laws [b], V.K. Peterson [c], J.O. Astbury [d], C.L. Wilson [d], S. Irukuvarghula [d], P.A. Burr [a]

[a] School of Mechanical and Manufacturing Engineering, University of New South Wales, Kensington, NSW 2052, Australia
[b] School of Materials Science & Engineering, University of New South Wales, Kensington, NSW 2052, Australia
[c] Australian Nuclear Science and Technology Organisation, Lucas Heights, Australia
[d] Tokamak Energy Ltd, 173 Brook Drive, Milton Park, Oxon OX14 4 SD, United Kingdom

ARTICLE INFO

Keywords:
ε tungsten boride
DFT simulations
Neutron diffraction

ABSTRACT

The ε-phase of tungsten boride, conventionally labelled as W2B5, has been identified as a promising candidate for shielding application in spherical tokamak fusion reactors. However, further research has been hindered by a lack of agreement on the structure and even composition of the ε-phase. Here, we identify the stable crystal structure and stoichiometry range of ε tungsten borides through a combination of *ab initio* simulations and neutron diffraction of isotopically enriched samples. We considered the ability to accommodate hypo-stoichiometry in six published structures of the ε phase. Chemical disorder was modelled using configurational ensembles to account for entropy of non-stoichiometry. We show that two W_2B_{4-x} structures (with x=~0.25 − 0.5), with space group symmetry $P6_3/mmc$ and $P6_3/mcm$, appear to be thermodynamically stable. These candidate compounds have 6.2 − 7.8 at.% less B than the W_2B_5 composition reported in exiting phase diagrams. We confirm these findings by means of neutron powder diffraction, performed on ^{11}B-enriched arc-melted and crushed samples. Rietveld refinement using the neutron data shows the ε-phase to be better described as $W_2B_{3.60(2)}$ ($P6_3/mcm$), in keeping with density functional theory (DFT) calculations. Linear change in DFT-derived lattice parameters of the candidates for the ε-phase proposes a simple model to assess the tungsten boride composition by measuring the lattice parameter (e.g. by X-ray diffraction. The simulations also reveal that the material can accommodate a range of stoichiometric variations (via B vacancies) with relatively small stored energy, which is a desirable feature for neutron shielding application.

1. Introduction

Tungsten borides have recently gained attention in the fusion industry as potential candidate high-performance radiation shielding materials [1–4]. They have a range of useful material properties, including high hardness, chemical inertness, resistance to thermal shock, and high temperature electrical resistance [5–13]. The nuclear properties of tungsten and boron, as well as the high density and large atomic number (Z) of tungsten, make tungsten borides effective shielding materials for attenuating both the neutron and gamma radiation produced in a fusion reactor [1]. This is advantageous for compact spherical tokamak fusion reactors where there is minimal clearance between the plasma vessel and the cryogenically-cooled superconducting magnets, which are sensitive to radiation damage and heat deposition from radiation [14–18].

The W-B phase diagram comprises 5 different binary phases – W_2B, WB, WB_2, W_2B_5 and WB_4 [19–24] Convention has labelled the ε tungsten boride phase as W_2B_5 [19]. According to the current phase diagram, phase-pure ε forms at approximately 68-70 at.% B. At higher at.% B, a binary mixture of the ε phase forms together with WB_4, while at lower at.% B the second component mixed in with the ε phase is WB [25]. The nominal stoichiometry of W_2B_5 for ε was identified as the best W-B phase for radiation shielding due its high boron content and high atomic density [1]. However, the exact stoichiometry of this phase is unclear, with reported boron content spanning 65–71.4 at.% B as W_2B_5 [19], WB_2 (W_2B_4) [26,27], $WB_{2.27}$ [28], W_2B_{5-x} [21], and W_2B_{4-x} [29]. The uncertainly in crystal structure and stoichiometry of this phase limits further study into its shielding performance, which is sensitive to atomic

* Corresponding author.
E-mail address: s.setayandeh@unsw.edu.au (S.S. Setayandeh).

https://doi.org/10.1016/j.actamat.2023.119282
Received 30 January 2023; Received in revised form 17 August 2023; Accepted 22 August 2023
Available online 23 August 2023

density and composition [1]. Similarly, simulation of radiation damage in this material, such as [31], necessitate an accurate description of the crystal structure.

Here, we aim to determine the crystal structure and stoichiometric range of the ε phase by combining *ab initio* calculations and neutron diffraction measurements of laboratory-prepared samples containing isotopically enriched B. We also propose a model to assess the tungsten boride composition by measuring the lattice parameter (e.g. by X-ray diffraction).

2. Methodology

2.1. Computational methods

All density functional theory (DFT) simulations were performed within the Vienna Ab-Initio Simulation Package (VASP) [30–32] with the Perdew, Burke, and Ernzerhof (PBE) exchange correlation functional [33]. The Projector Augmented Wave (PAW) pseudo-potentials [34,35] from the VASP 5.3 repository were employed to describe the B and W atoms, with three and six valence electrons respectively, and a consistent plane-wave energy cut-off of 400 eV. The electronic wave functions were sampled within the Brillouin zone, using a Monkhorst-Pack [36] k-point grid with a density as close as possible to 31.4 Å, and never lower than 25.9 Å in all reciprocal directions. A first-order Methfessel-Paxton smearing function of width 0.1 eV [37] was applied to treat partial occupancies of bands. All simulations were energy minimised at constant pressure (atomic positions and lattice vectors were allowed to relax). The convergence criteria for ionic and electronic minimisation were set to 10^{-5} eV and 10^{-6} eV, respectively.

Our previous work proposed that the ε phase might be non-stoichiometric, possibly a hypo-stoichiometric form of W_2B_{5-x} [38]. To investigate this possibility, we considered deviation of stoichiometry in two reported stoichiometric polymorphs of tungsten boride with the W_2B_5 composition (tri and hex^2 in Fig. 1) [38]. Although W_2B_5 (tri) was found to be metastable, this structure was also considered as it is only slightly above the convex hull in Fig. 1. The convex hull line connects the lowest energy compounds in a composition range, such that a compound that does not lie on it, is not thermodynamically stable. We also considered the first experimental report for the ε-phase [19], labelled as W_2B_5 (hex^1) in this study.

Furthermore, we investigated the possibility of the ε phase to be hypo-stoichiometric W_2B_{4-x} by considering deviation of stoichiometry in three stoichiometric polymorphs of tungsten boride with the W_2B_4 composition. These polymorphs are hex^1 and hex^2 shown in Fig. 1, and hex^3 reported by [29].

Hypo-stoichiometric variations of these stoichiometric structures were generated by introducing B vacancies to perfect 3*3*1, 2*2*1, and 2*1*1 supercells of these candidates. We considered both ordered and disordered accommodation of hypo-stoichiometry by simulating all symmetrically-unique permutations of B vacancy configurations, and then treated them as configurational ensembles which yield exact thermodynamic averages [39]. This approach can lead to a prohibitively large number of simulations when the number of vacancies is large, for example, for a W_2B_{5-x} structure with the $P6_3/mmc$ space group and $x = 0.22$ (4 vacancies in a 126-atom supercell) there are more than 10000 configurations to model. Thus, to achieve greater level of hypo-stoichiometry, we also used a complementary approach where vacancies were introduced to one sublattice at a time (again, all configurations within that sublattice were modelled. This approach informed us on the relative ability of each B sublattice to accommodate vacancies. A comparison of the two approaches at lower x is used to validate that mixed-sublattice configurations are rarely more energetically favourable than single sublattice configurations, and that the energy difference is small anyway. In a configurational ensemble [39] the effective formation enthalpy of a compound was calculated as:

$$E_{eff} = \sum_{n=1}^{N} P_n E_n^f \tag{1}$$

where P_n is the ensemble probability of occupying a particular configuration with formation enthalpy of E_n^f.

The ensemble probability at temperature T was calculated as:

$$\boldsymbol{P_n} = \frac{\boldsymbol{\Omega_n} \exp\left(\frac{-E_n^f}{k_B T}\right)}{\sum_{n=1}^{N} \boldsymbol{\Omega_n} \exp\left(\frac{-E_n^f}{k_B T}\right)} \tag{2}$$

where Ω_n and k_B indicate the number of symmetrically equivalent states and Boltzmann constant, respectively. Symmetrically unique configurations were identified by the site occupation disorder (SOD) code [40].

The formation enthalpy of a phase was calculated as:

$$\boldsymbol{E_n^f} = \frac{\boldsymbol{\mu}(W_n B_m) - \boldsymbol{n}\boldsymbol{\mu}(W) - \boldsymbol{m}\boldsymbol{\mu}(B)}{\boldsymbol{n} + \boldsymbol{m}} \tag{3}$$

where μ is the chemical potential, here taken as half the DFT energy of the body-centred cubic -W unit cell and one thirty-sixth of the DFT energy of α-rhombohedral B.

The Gibbs free energy of formation at any given temperature T was calculated as:

$$G_f = E_{eff} - TS^{conf} \tag{4}$$

where S^{conf} is configurational entropy calculated as:

$$S^{conf} = K_B \sum_{n=1}^{N} P_n \ln P_n \tag{5}$$

As the candidate structure display disorder, and all reactants and products are consistent for all reactions considered here, with no gaseous species a no spin-polarised phases, we expect the entropy term to be dominated by configurational disorder. Due to the practical limitation, the vibrational entropy is not included.

The same approach was employed to calculate the effective lattice constant of each compound.

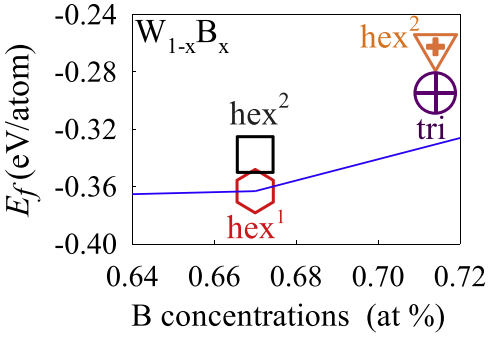

Fig. 1. Convex hull diagram of the W-B system, obtained with the PBE exchange correlation functional (extracted from ref. [38]).

2.2. Experimental methods

Tungsten boride was synthesized from solid tungsten rods (99.95 wt. %) powderised to a size of 10-20 μm and crystalline ^{11}B-enriched boron powder (3M™, 99.998 wt.% chemical purity, 99.62 at.% isotopic purity). These were mass-balanced to achieve a target stoichiometry of 68 at.% B and 32 at.% W. The materials were blended and mechanically pressed into a pellet, which was then placed on a water-cooled copper hearth within the enclosed chamber of an arc melting furnace, together with a sacrificial pellet of titanium metal. The enclosed chamber was evacuated and back-purged with high purity argon gas (99.999 vol.% purity) several times to ensure minimal air/oxygen remained in the

melting chamber, with a final high vacuum purge of less-than 10^{-5} mbar. To mitigate oxidation during arc melting, a titanium button was melted separately using an electric arc. An electric arc was then used to alloy the tungsten and boron into a solid button on the copper hearth. To ensure homogeneity the button was remelted at least 5 times, flipping it between melt cycles. After alloying, the button was weighed to ensure the target mass balance was retained.

The sample was ground into a fine powder using an agate motor and pestle. X-ray powder diffraction (XRD) patterns were collected on the powder on a PANalytical Aeris powder diffractometer using Cu Kα radiation. High-resolution neutron powder diffraction (NPD) data were obtained on Echidna at the Australian Nuclear Science and Technology Organisation (ANSTO) [41,42]. The powder was packed in a 6 mm diameter vanadium can and measured at room temperature at two wavelengths of 1.62131(3) Å and 2.43842(5) Å, as determined from data for the $La^{11}B_6$ 660b standard reference material from the national institute of standards and technology [43] which was also used to determine instrument contributions to the data. Rietveld analysis was performed using GSAS-II [44]. The coherent neutron scattering factors of W (4.86 fm) and ^{11}B (6.65 fm) are comparable [45], which make it possible to probe the positions and occupancies of the lighter (low Z) B atoms among heavier (high Z) W atoms.

The neutron diffraction data collected at the two wavelengths were used in a co-refinement of the structure, with instrumental sample displacements constrained to be the same. To account for sample absorption, an absorption coefficient for each wavelength was calculated using the NIST neutron activation and scattering calculator and the value fixed throughout the refinement [46]. The instrumental contributions to peak broadening and peak asymmetry were fixed throughout the refinements to values obtained from the $La^{11}B_6$ 660b standard reference material under the same instrumental configuration. The background contribution to the data was modeled using a Chebyshev function with 7 and 4 terms for the datasets collected at ~ 1.62 Å and ~ 2.44 Å, respectively. Due to high correlation between the background coefficients and atomic displacement parameters, background coefficients were initially refined and then fixed during the refinement before being allowed to refine again during convergence in the global minimum along with the sample displacement parameters parallel and perpendicular to the neutron beam, histogram scale factors, scale factors for the minor phases, and unit cell parameters of all phases.

For the primary tungsten boride phase, the site occupancy of the W atom was fixed to 1 and the atomic displacement parameters for the B atoms were constrained to be equal and modelled isotropically. The atomic coordinates, site occupancies, and isotropic atomic displacement parameters of the final W_2B_{4-x} phase were refined along with peak broadening arising from micro-strain. Further details of the refinement analysis can be found in Table S1 of the supporting information.

The neutron diffraction data could be indexed by four phases: W_2B_{4-x} (hex^2 or hex^3), WB_4 ($P6_3/mmc$), SiB_6 ($Pm\bar{3}m$), and SiO_2 ($P3_221$). The hex^2 and hex^3 models identified from the DFT simulations were used as starting points for the W_2B_{4-x} phase, while starting models for the other phases were obtained from the ICSD database [26,28,47,48].

The sample was imaged using a Hitachi S3400 scanning electron microscope. Energy dispersive spectroscopy (Bruker Esprit) was used for further phase identification.

3. Results

3.1. Thermodynamic stability

Crystal structures of W_2B_5 (hex^1), W_2B_5 (hex^2), and W_2B_5 (tri) are depicted and described in Fig. 2 and Table 1, respectively. The average formation enthalpies of hypo-stoichiometric W_2B_{5-x}, calculated with eqn. 1 at T = 50 K, are illustrated in Fig. 3. The effect of ensemble temperature was found to be negligible and is shown in the supporting information (Figure S1). Each point corresponds to the ensemble average of all vacancy configurations at that composition and is the results of over a hundred thousand DFT simulations, where the lowest energy configurations have the greatest weight. Each row of graphs shows the effect of increasing hypo-stoichiometry (x) to one of the three starting stoichiometric W_2B_5 structures. The panels on the left show the results of adding vacancies to one B sublattice at a time, while the panels on the right show the average energy when vacancies are not constrained to one sublattice (but naturally include all configuration where B are relegated to one sublattice).

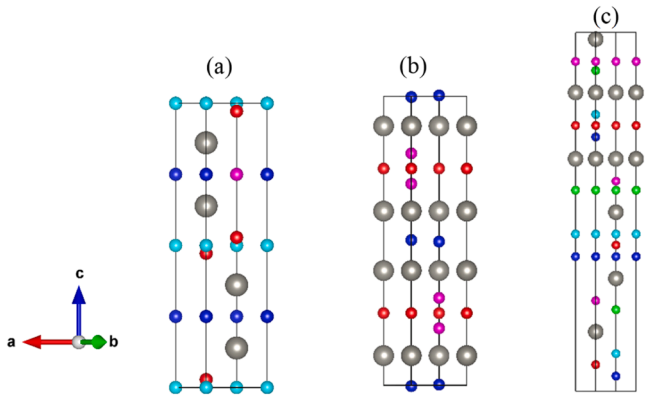

Fig. 2. Crystal unit cells of (a) W_2B_5 (hex^1) [49], (b) W_2B_5 (hex^2), [50] and (c) W_2B_5 (tri) [51]. Large grey spheres are W and small spheres are B. Different B sublattices are colour coded. Structures with the same crystal class and different motif are indicated by a superscript (^{1} and ^{2}).

Table 1
Crystal structure definition of stochiometric W_2B_5 compounds reported of the ε-phase of tungsten boride.

Name and space group	Lattice Parameter (Å)	Wyckoff positions Atom	x	y	z	Ref.
hex^1 ($P6_3/mmc$)	a = 2.982 c = 13.87	W1 (4*f*) B1 (2*b*) B2 (2*d*) B3 (4*f*) B4 (2*a*)	0.333333 0.000000 0.333333 0.000000	0.666667 0.000000 0.666667 0.000000	0.139000 0.250000 0.750000 -0.028000 0.000000	[49]
hex^2 ($P6_3/mmc$)	a = 3.0171 c = 15.7082	W1 (4*e*) B1 (2*b*) B2 (4*f*) B3 (4*f*)	0.000000 0.000000 0.333333 0.333333	0.000000 0.000000 0.666667 0.666667	0.397090 0.250000 0.302580 0.497260	[50]
tri ($R3m$)	a = 2.9225 c = 5.9018	W1 (3*a*) W2 (3*a*) B1 (3*a*) B2 (3*a*) B3 (3*a*) B4 (3*a*) B5 (3*a*)	0.666667 0.666667 0.333333 0.333333	0.333333 0.333333 0.666667 0.666667	0.981200 0.165900 0.074200 0.252500 0.042200 0.104900 0.227300	[51]

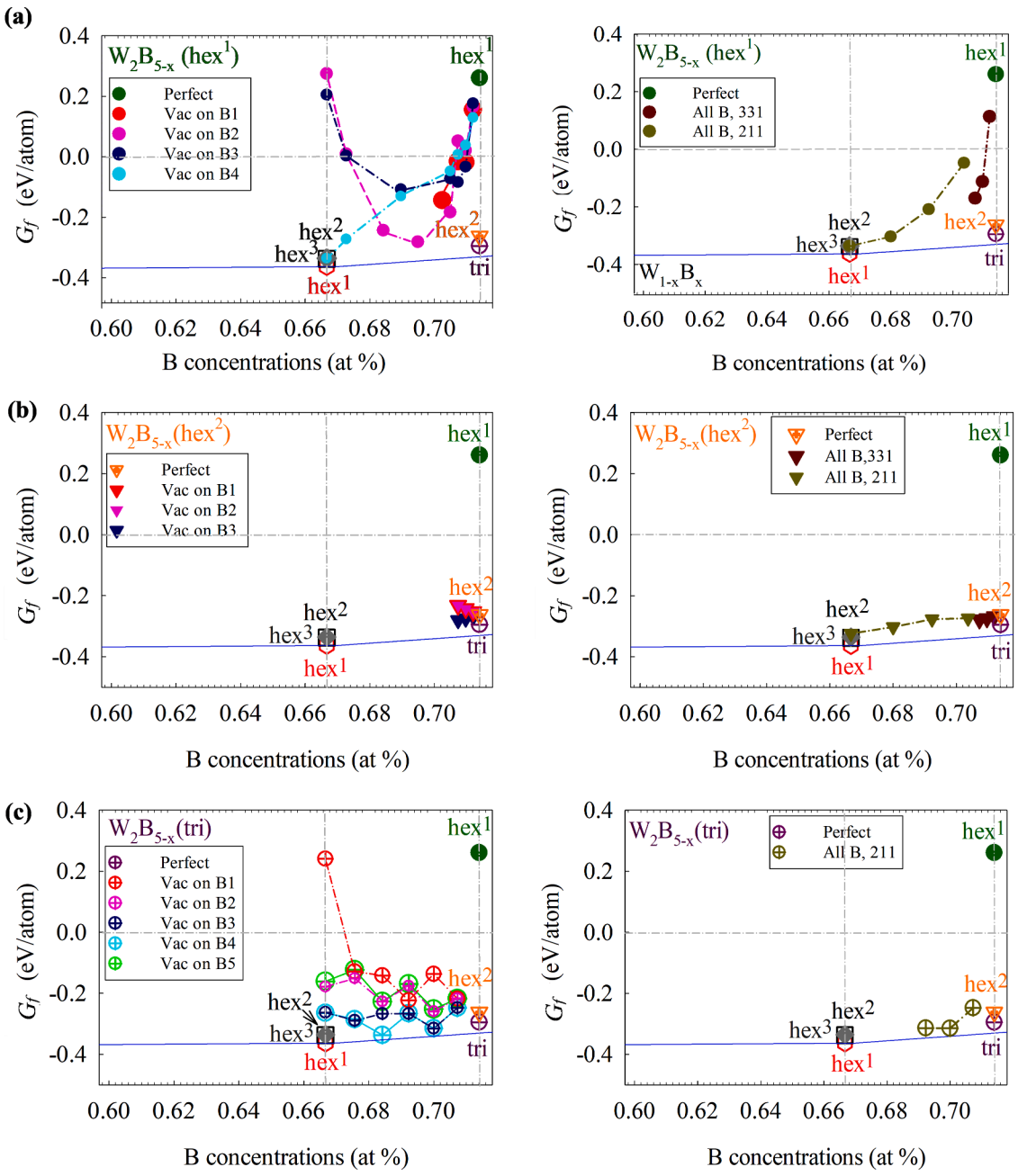

Fig. 3. Formation Gibbs free energy of a) W_2B_{5-x} (hex^1), b) W_2B_{5-x} (hex^2), and c) W_2B_{5-x} (tri) compounds. Left and right panels represent the compositions obtained via introducing B vacancies in only one B sublattice each time, and in all B sublattices, respectively. The blue line represents the convex hull. Dashed lines through the points are a guide to the eye.

For W_2B_5 (hex^1), increasing hypo-stoichiometry (x) reduces the formation enthalpy dramatically. However, none of the W_2B_{5-x} (hex^1) data cross the convex hull in the composition range of ~ 67-71.4%. For W_2B_5 (hex^2) and W_2B_5 (hex^3), increasing hypo-stoichiometry does not have any significant effect on the formation enthalpy, and consequently none of these modelled compositions lay on the convex hull. This points out that amongst the candidates and the configurations we considered and within the limits of our approach, there is no stable W_2B_{5-x} structure. We note, however, that W_2B_{5-x} appears to be more stable than W_2B_5 and less stable than W_2B_4. This implies that the ε-phase might be a hypo-stochiometric W_2B_{4-x} phase.

An interesting observation is that for W_2B_5 (hex^1), all B sublattices energetically compete to accommodate B vacancies at higher B content. This indicates that it is likely for B vacancies to form on multiple sublattices. This is confirmed in Fig. 3 (a, right), where similar energies are observed despite the B vacancies not being constrained to a single sublattice.

Fig. 5 represents the formation enthalpies of hypo-stoichiometric models of polymorphs W_2B_4 (hex^1), W_2B_4 (hex^2), and W_2B_4 (hex^3), calculated via eqn. 1 at T = 50 K. Again, the effect of averaging temperature is presented in the supporting information (Figure S2). Interestingly, five hypo-stoichiometric models were found to be stable, in the composition range of 63.6 – 65.2 at.% B, corresponding to $W_2B_{3.5\text{-}3.75}$. Three of these five are hypo-stoichiometric models of the polymorph W_2B_4 (hex^2). These models correspond to $W_2B_{3.75}$ (~ 65.22 at.% B, with sites 4f, 2d, and 2b occupancies of 0.99, 0.99, and 0.77, respectively), $W_2B_{3.63}$ (~ 64.44 at.% B, with sites 4f, 2d, and 2b, occupancies of 0.75, 0.98, and 0.90, respectively) and $W_2B_{3.5}$ (~ 63.64 at.% B, with site 4f

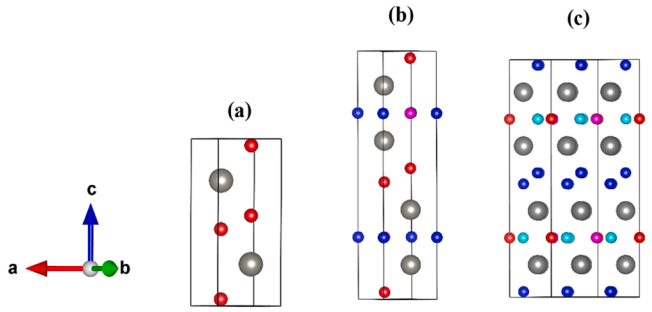

Fig. 4. Illustrates crystal structures of W_2B_4 (hex^1), W_2B_4 (hex^2), and W_2B_4 (hex^3). A description of these structures is presented in Table 2. Figure 4. Crystal unit cells of (a) W_2B_4 (hex^1) [50], (b) W_2B_4 (hex^2) [26], and (c) W_2B_4 (hex^3) [29]. Grey/large spheres are W and coloured/small spheres are B. Different B sublattices are colour coded. Variations of the crystal with the same space group and different motif are indicated by a superscript.

and 2b occupancies of 0.99 and 0.75, respectively). The two remaining models are hypo-stoichiometric models of the polymorph W_2B_4 (hex^3), and in both cases the B vacancies are accommodated only on the 2a B sublattice: in one case partially, corresponding to $W_2B_{3.71}$ (~ 65 at.% B, with site 2a occupancy of 0.125) and in the other case fully, corresponding to $W_2B_{3.67}$ (64.7 at.% B). None of the hypo-stoichiometric variations of the polymorph W_2B_4 (hex^1) were found to be stable.

Table 2

3.2. X-ray diffraction

Initial phase identification was carried out with laboratory XRD, and the data is presented in the supporting information. No reflections corresponding to the previously reported trigonal phase (space group $R\bar{3}m$) were observed [12]. Both $P6_3/mmc$ (hex^2) and $P6_3/mcm$ (hex^3), as identified from the DFT calculations, appear to be valid candidate space groups, noting that the XRD signal is overwhelmingly dominated by the W positions and occupancies, which are similar in the proposed models for both space groups. The powder was found to contain small amounts of WB_4 ($P6_3/mmc$, 7 ± 1 wt.%), SiB_6 ($Pm\bar{3}m$, 13 ± 1 wt.%) and SiO_2 ($P3_221$, 6 ± 1 wt.%) impurities, noting that XRD is more surface-sensitive while NPD is more representative of the bulk average. The secondary phases present indicates that the target stoichiometry of 68 at.% B and 32 at.% W resulted in excess B, which formed WB_4, while the Si-containing phases are likely impurities from crushing and grinding the sample [24].

3.3. Neutron diffraction

With the hex^2 structural model (Table S2), in addition to the WB_4 ($P6_3/mmc$), SiB_6 ($Pm\bar{3}m$), and SiO_2 ($P3_221$) secondary phases, a poor fit to the data was obtained. As shown in the supporting information (Figure S4) there exist several small reflections (Q ≅ 1.36, 1.64, 2.26, 2.92, 3.79, 3.88, 5.06, 6.09, 7.09, 7.33 Å^{-1}) that are not accounted for. In contrast, the hex^3 model (Table S3) proposed by the DFT calculations (in addition to the minor impurity phases) accounts for all the reflections observed in the NPD data.

The Rietveld refined fits of the W_2B_{4-x} (hex^3) structural model are

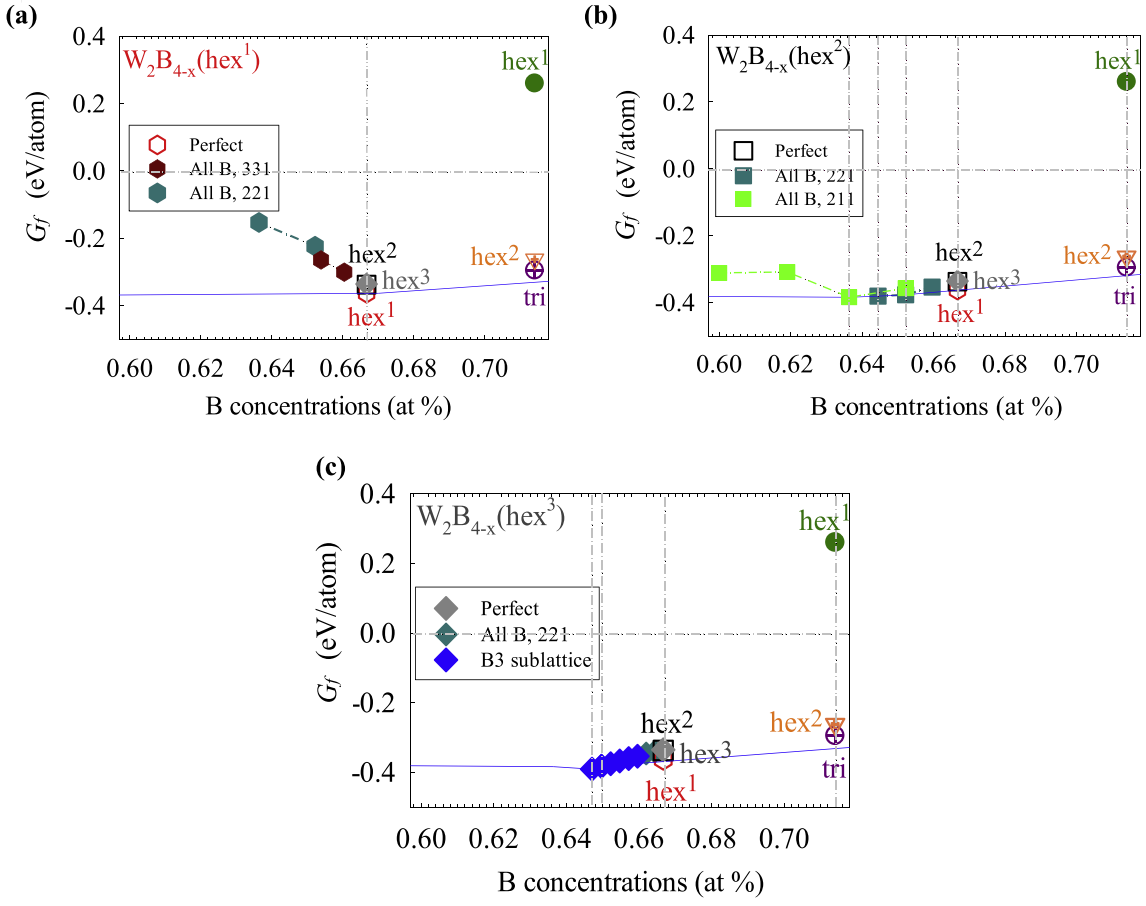

Fig. 5. Formation Gibbs free energy of a) W_2B_{4-x} (hex^1), b) W_2B_{4-x} (hex^2), and c) W_2B_{4-x} (hex^3) compounds obtained via introducing B vacancies. The blue line represents the convex hull and dashed lines through the points are a guide to the eye.

Table 2
Crystal structure definition of stoichiometric W_2B_4 compounds reported for the ε-phase of tungsten boride.

Comp.	Space group	Lattice Parameter (Å)	Wyckoff positions Atom	x	y	z	Ref.
W_2B_4	hex[1] ($P6_3/mmc$)	a = 2.926900	W (2*c*)	0.333333	0.666667	0.250000	[50]
		c = 7.750700	B (4*f*)	0.333333	0.666667	0.540730	
	hex[2] ($P6_3/mmc$)	a = 2.984000	W1 (4*f*)	0.333333	0.666667	0.139000	[26]
		c = 13.870000	B1 (4*f*)	0.333333	0.666667	-0.028000	
			B2 (2*d*)	0.333333	0.666667	0.750000	
			B3 (2*b*)	0.000000	0.000000	0.250000	
	hex[3] ($P6_3/mcm$)	a = 5.174200	W (12*k*)	0.667100	0.000000	0.363400	[29]
		c = 13.896000	B1 (2*a*)	0.000000	0.000000	0.250000	
			B2 (4*c*)	0.333333	0.666667	0.250000	
			B3 (12*k*)	0.666300	0.000000	0.523200	
			B4 (6*g*)	0.325300	0.000000	0.250000	

shown in Fig. 6 and the corresponding crystallographic details are given in Table 3. The structural information of particular interest (B site occupancy factors), in addition to atomic positions and atomic displacement parameters, is contained within the relative peak intensities of the NPD pattern. These crystallographic parameters can be highly correlated. For example, atomic displacement parameters that are too large can be compensated for by reduced site occupancies. Similarly, allowing both parameters to refine freely can lead to changes in the values without improving the overall fit of the Rietveld model to the data. To test the sensitivity of B site occupancies to the atomic displacement parameters, the change in B stoichiometry (x in W_2B_{4-x}) and quality of fit through the weighted-profile R-factor (wRp), as a function of the

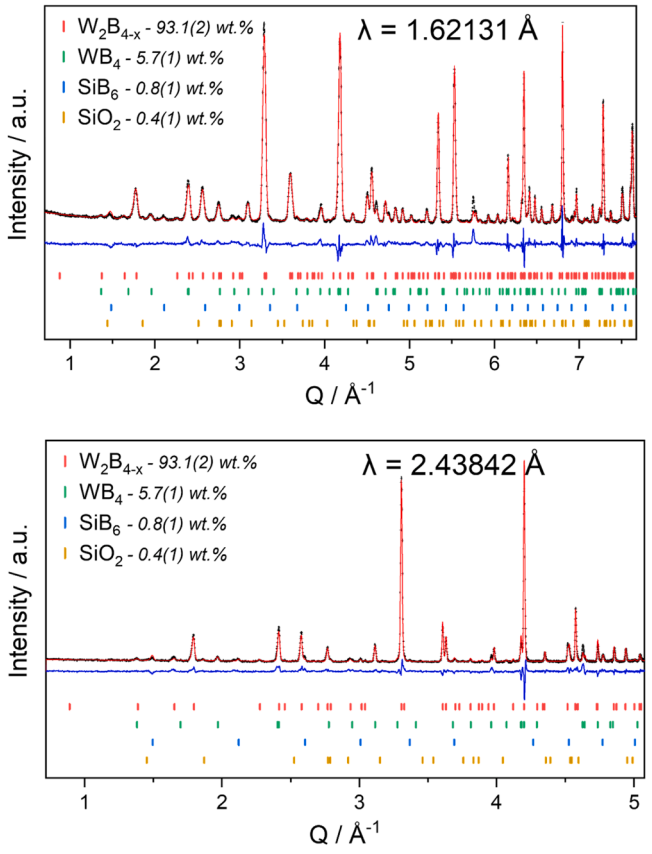

Fig. 6. Rietveld refinement profiles using NPD data for the W_2B_{4-x} sample collected at 1.62131(3) Å and 2.43842(5) Å. Measured data are shown as black crosses where standard uncertainties are represented by the length, the calculated Rietveld model is shown as a solid red line through the data and the difference between the data and the model as the blue line below. A linear scale is used for both axes. Vertical markers show the positions of allowed Bragg reflections for the phases identified inset.

Table 3
Crystallographic parameters for $W_2B_{3.60(2)}$ as determined from Rietveld analysis of NPD data.

Atom	Site	x	y	z	SOF	$U_{iso} \times 100$ / Å^2
W	12*k*	0.6689(9)	0	0.3627(1)	1	0.13(4)
B	2*a*	0	0	1/4	0.14(1)	0.20(2)
B	4*c*	1/3	2/3	1/4	0.94(1)	0.20(2)
B	12*k*	0.6661(5)	0	0.5227(1)	0.99(1)	0.20(2)
B	6*g*	0.3242(9)	0	1/4	0.95(1)	0.20(2)

Space group $P6_3/mcm$, $wR_p = 6.3\%$, $a = b = 5.1740(1)$ Å, $c = 13.8966(2)$ Å

isotropic atomic displacement (U_{iso}) were evaluated. The results presented in Figure S5 of the supporting information demonstrate that a reduction in U_{iso} (and decrease in B site occupancy) improves the quality of fit, up to a U_{iso} value of approximately 0.25. Therefore, reasonable B U_{iso} (0.002(2)) values were obtained in the final refinement, adding certainty to the $W_2B_{3.60(2)}$ composition determined via Rietveld refinement using the NPD data. This is the only solution that yields an acceptable fit to the data.

3.4. SEM/EDS

SEM images showing the particle size and morphology and of the ground tungsten boride sample can be found in the supporting information. A range of particles sizes from 5 μm to 240 μm are present in the sample. From the EDS analysis, three phases were detected – SiO_2, a W-rich WB phase and W-poor WB phase. From the XRD and NPD, the W and B-containing phases are $W_2B_{3.6}$ and WB_4. For future studies, samples will be characterized in bulk before producing the powdered sample.

3.5. Lattice parameter change

Fig. 7 illustrates the configurational average lattice strain (at T = 50 K) with changes in stoichiometry of W_2B_{4-x} (hex[3]), with respect to the average lattice parameters of the stochiometric W_2B_4 (hex[3]). The effect

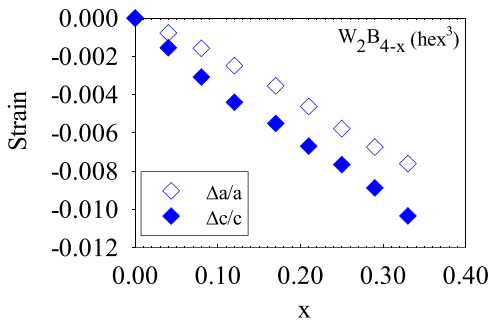

Fig. 7. DFT-derived lattice strain (at T = 50 K) with changes in stoichiometry of W_2B_{4-x} (hex[3]).

of ensemble temperature was found to be negligible. A near-linear increase is observed in lattice constants with increasing boron content. Noting, however, the lattice parameter changes along *a* and *c* axes are not isotropic. Calibrating these strains with the neutron diffraction-measured lattice constants at a boron content of 64.29 at.% corresponding to x = 0.4, following relationship was found for the *a* and *c* lattice parameters as a function of *x*:

$$\begin{cases} a = 5.18344 - 0.02360 * x \\ c = 13.90856 - 0.0299 * x \end{cases} \quad (6)$$

4. Discussion

Experimental studies of the ε-phase suggest different crystal structures. X-ray powder diffraction first performed by Kiessling *et al.* [19] found a W_2B_5 composition with a hexagonal crystal structure and space group $P6_3/mmc$ (labelled as W_2B_5 (hex^1) here). Due to subtle variations in the observed $\sin^2\theta$ values compared to values for the ideal stoichiometry, B in the ε-phase was estimated at 66.7 at.% B [19]. Determining the positions and occupancies of B atoms from X-ray data is challenging due to the overwhelming signal from W atoms. The ε-phase continued to be described as W_2B_5.

Frotscher *et al.* in 2007 [26], performed DFT calculations and proposed a similar hexagonal structure with space group $P6_3/mmc$(labelled as W_2B_4 (hex^2) here), where one boron sublattice removed. Kayhan *et al.* performed neutron diffraction experiments in 2013 [29] and proposed a new structure with additional B vacancies: W_2B_{4-x} with a $P6_3/mcm$ space group (labelled as W_2B_4 (hex^3) here). Neutron scattering lengths of ^{11}B and W are comparable in scale (6.65 and 4.86 fm, respectively), so the structure factors are sensitive to B. However, the peak intensities analysed by Kayhan *et al.* [29] were influenced by texture, which made the result inconclusive. Gu *et al.* [52] carried out more recent neutron diffraction studies using a high-pressure method and reported a stoichiometry equivalent to $W_2B_{4.68}$, with space group $P6_3/mmc$, [52].

DFT simulations [50,53] suggested additional structures, by assessing the ground state formation energy of undefective, stoichiometric crystals. Previously [38], we compared all reported stoichiometric polymorphs of tungsten boride with compositions in the range of 50–80 at.% B. The thermodynamic stability of these structures was then considered via calculating their formation free energies. Seven candidates were found to be mechanically, dynamically and thermodynamically stable [38]. Four possess hexagonal or trigonal crystal structures (W_2B_5 (tri), W_2B_5 (hex^2), W_2B_4 (hex^1), and W_2B_4 (hex^2)) that could match diffraction measurements. The formation energies of these polymorphs are shown in Fig. 1. Among these W_2B_5 (tri) and W_2B_5 (hex^2) were found to be metastable and the ε-phase a non-stoichiometric variation of the previously reported structures [38].

Hypo-stoichiometry leads to a marked reduction in energy of W_2B_5 (tri), W_2B_5 (hex^1), and W_2B_5 (hex^2), but this is still insufficient to reach the convex hull between W_2B_4 and W_2B_5. However, W_2B_{5-x} appears to be more stable than W_2B_5 and less stable than W_2B_4. This suggests the possibility of the ε-phase to be a hypo-stoichiometric W_2B_{4-x}. Reducing the stoichiometry further to W_2B_{4-x}, commencing from W_2B_4 (hex^1), W_2B_4 (hex^2), and W_2B_4 (hex^3), identifies five stable hypo-stoichiometric models. These results imply that the ε-phase is most likely a hypo-stoichiometric W_2B_{4-x} with hexagonal crystal structure and space group either $P6_3/mmc$ or $P6_3/mcm$ and total B content in the range 3.50 − 3.75.

To experimentally determine the structure and stoichiometry of the ε-phase, a sample was prepared by arc-melting tungsten and boron. While XRD and SEM/EDS provide insights into the phase composition, the XRD pattern is dominated by scattering from the heavier W atoms and SEM/EDS is not reliable for quantitative measurements of light elements, including B. Therefore, neutron diffraction was necessary to probe the positions and occupancies of both W and B in the ε-phase and so the sample had to be made using isotopically enriched B-11 instead of natural B, which has a high neutron absorption cross section.

The same phases (W_2B_{4-x}, WB_4, SiB_6 and SiO_2) were identified in both the XRD and NPD analyses. Some variation was observed in the phase fractions between the XRD and NPD analyses, with the XRD data being more surface-sensitive compared to NPD. Notably, only the NPD data could be used to distinguish between the two possible space group symmetries ($P6_3/mmc$ or $P6_3/mcm$) and determine the W:B stoichiometry for the ε-phase. Comparable lattice parameters were obtained for the ε-phase from both XRD (5.1742(1) Å, 13.8957(2) Å) and NPD (5.1740(1) Å, 13.8966(2) Å).

In agreement with the results of the DFT calculations, the neutron data show that the B 2*a* (B1) site in the hex^3 structure has a low occupancy of 0.13(1). DFT modeling revealed possible occupancies of 0.125 and 0 for the B 2*a* site. Neutron refinement reveals vacancies on the B 4c and 6g sites, which were assumed fully occupied in DFT calculations, resulting in a lower stoichiometry of $W_2B_{3.60(2)}$ compared to $W_2B_{3.67\text{-}3.71}$ suggested by DFT for the hex^3 structure.

The $W_2B_{3.60(2)}$ stoichiometry determined from the NPD data is lower than the nominal composition ($W_2B_{4.25}$) based on the stoichiometry of starting reagents. Some boron loss, through spattering and evaporation, is expected during the arc melting process. However, the total B content accounted for by the Rietveld analysis across all phases corresponds to a stoichiometry of $W_2B_{4.03(1)}$, which is significantly higher than the possible range of stoichiometries (W_2B_{4-x}, $0.25 \leq x \leq 0.5$) identified by DFT, as well as the $W_2B_{3.60(2)}$ composition confirmed by NPD. The formation of hypo-stoichiometric $W_2B_{3.60(2)}$, despite the presence of excess B, strongly indicates that the boron content in the ε-phase of tungsten boride is substantially lower than previously reported. In keeping with the existing W-B phase diagram, the excess boron is accommodated by the boron-rich WB_4 phase [54]. Variations in B-content of the ε-phase are expected, and further work will be carried out to determine the equilibrium ε-phase composition range boundaries.A near-linear increase between lattice parameters and B content was predicted by the DFT simulations. Applying this relationship to the NPD-measured lattice parameters, we propose a model (eqn. 4) to assess the tungsten boride composition by measuring the lattice parameter (e.g. by X-ray diffraction). Noting, however, the accuracy of this model is clearly affected by limits of our approach and the calibration data employed, but nevertheless the trends of lattice parameter with increasing the B content is evident, reinforcing the capability of the model.

Conclusions

DFT calculations explored reducing the B stoichiometry of W2B5 structures, revealing insufficient stability improvement. Further reducing the stoichiometry to W2B4-x resulted in stable hypo-stoichiometric models (W:B ratio of 2:3.50−2:3.75) with space groups P63/mmc and P63/mcm. NPD data confirmed the W2B3.60(2) composition, validating one of the DFT models. To gather NPD data, the ε-phase of tungsten boride (nominally 68 at.% B) was prepared by arc melting W chips with isotopically enriched ^{11}B powder. The best fit of the NPD data was obtained with a $P6_3/mcm$ structural model and $W_2B_{3.60(2)}$ composition, verifying one of the models identified from the DFT calculations. The refined model contains a largely vacant *2a* sublattice (0.14(1) occupancy), while the other three B sites retain occupancies above 0.94. The lower B content of the ε-phase explains the formation of B-rich secondary phases, despite some loss of B powder during arc-melting.

We propose a numerical model that predicts the lattice parameter as a function of deviation of stoichiometry, using the predicted lattice strains from DFT and calibrating them with the NPD refined lattice parameters. The model can be used in reverse to calculate the stoichiometry for simple lattice parameter measurements, without the need for neutron scattering and B-11 enriched samples.

The combined approach of DFT calculations and neutron diffraction

provides -substantial evidence that the atomic content of B in the tungsten boride ε-phase (63.6 − 65.2 at.% B) is substantially lower than the previously reported values of 71.4 at.% B (W_2B_5), and even lower than 66.7 at. % B (W_2B_4). The newfound $W_2B_{3.60(2)}$ stoichiometry will enable more accurate determination of the materials performance parameters, in turn aiding the design and development of fusion reactors. As a final remark, we note that the tungsten-boron phase diagram should be revisited to account for the substantial discrepancy in the ε-phase composition.

Declaration of Competing Interest

The authors declare that they have no known competing financial interests or personal relationships that could have appeared to influence the work reported in this paper.

Acknowledgements

SSS, PAB, MIB, JHS and EGO would like to acknowledge Tokamak Energy (UK) for providing financial support. MB acknowledges Tyree foundation for providing financial support. This research was supported by an Australian Government Research Training Program (RTP) Scholarships. This work was undertaken with the assistance of resources and services from the National Computational Infrastructure (NCI), which is supported by the Australian Government; the Pawsey Supercomputing Centre, which is supported by the Australian Government and the Government of Western Australia; and was enabled by Intersect Australia Limited (www.intersect.org.au). Part of this research was undertaken on the Echidna beamline at the Australian Centre for Neutron Scattering, ANSTO, under proposal MI13195.

Supplementary materials

Supplementary material associated with this article can be found, in the online version, at doi:10.1016/j.actamat.2023.119282.

References

[1] C.G. Windsor, et al., Tungsten boride shields in a spherical tokamak fusion power plant, Nucl. Fus. (8) (2021) 61.
[2] C.G. Windsor, et al., Activation and transmutation of tungsten boride shields in a spherical tokamak, Nucl. Fus. 62 (3) (2022).
[3] C.G. Windsor, et al., Design of cemented tungsten carbide and boride-containing shields for a fusion power plant, Nucl. Fus. 58 (7) (2018).
[4] M. Athanasakis, et al., A high temperature W2B–W composite for fusion reactor shielding, J. Nucl. Mater. (2020) 532.
[5] N. Gonzalez Szwacki, The structure and hardness of the highest boride of tungsten, a borophene-based compound, Sci. Rep. 7 (1) (2017) 4082.
[6] V. Funke, S. Yudovskii, G. Samsonov, Hard Alloys, Metallurgizdat 92 (1962) 4.
[7] V.I. Matkovich, G. Samsonov, P. Hagenmuller, Boron and refractory borides, Springer, 1977.
[8] S. Yazici, Bora Derin, Double SHS of W2B5 powder from CaWO4 and B2O3, Adv. Sci. Technol. 63 (2010) 246–250.
[9] E. Zhao, et al., Phase stability and mechanical properties of tungsten borides from first principles calculations, Phys. Chem. Chem. Phys. 12 (40) (2010) 13158–13165.
[10] R.F. Zhang, et al., Stability and strength of transition-metal tetraborides and triborides, Phys. Rev. Lett. 108 (25) (2012), 255502.
[11] H. Gou, et al., Peculiar structure and tensile strength of WB4: nonstoichiometric origin, AIP Advances 2 (1) (2012).
[12] Y. Liang, X. Yuan, W. Zhang, Thermodynamic identification of tungsten borides, Phys. Rev. B 83 (22) (2011).
[13] A.G. Kvashnin, et al., New tungsten borides, their stability and outstanding mechanical properties, J. Phys. Chem. Lett. 9 (12) (2018) 3470–3477.
[14] C.G. Windsor, et al., Modelling the power deposition into a spherical tokamak fusion power plant, Nucl. Fusion. 57 (3) (2017).
[15] M. Windridge, Smaller and quicker with spherical tokamaks and high-temperature superconductors, Philos. Trans. A Math. Phys. Eng. Sci. 377 (2141) (2019), 20170438.
[16] S.A. Humphry-Baker, G.D.W. Smith, Shielding materials in the compact spherical tokamak, Philos. Trans. A Math. Phys. Eng. Sci. 377 (2141) (2019), 20170443.
[17] A. Sykes, et al., Compact fusion energy based on the spherical tokamak, Nucl. Fus. 58 (1) (2018).
[18] C.G. Windsor, J.G. Morgan, P.F. Buxton, Heat deposition into the superconducting central column of a spherical tokamak fusion plant, Nucl. Fusion. 55 (2) (2015).
[19] R. Kiessling, et al., The crystal structures of molybdenum and tungsten borides, Acta Chem. Scand. 1 (1947) 893–916.
[20] H. Itoh, et al., Formation process of tungsten borides by solid state reaction between tungsten and amorphous boron, J. Mater. Sci. 22 (8) (1987) 2811–2815.
[21] S. Okada, K. Kudou, T. Lundström, Preparations and some properties of W2B, δ -WB and WB2 crystals from high-temperature metal solutions, Japan. J. Appl. Phys. 34 (Part 1) (1995) 226–231. No. 1.
[22] Woods, H.P., F.E. Wawner, Jr., and B.G.J.S. Fox, Tungsten diboride: preparation and structure. 1966. 151: p. 75.
[23] M. Kayhan, et al., Neutron diffraction and observation of superconductivity for tungsten borides, WB and W2B4, Solid State Sci. 14 (11) (2012) 1656–1659.
[24] Mohammadi, R., et al., Tungsten tetraboride, an inexpensive superhard material. 2011. 108(27): p. 10958-10962.
[25] M. Usta, et al., The characterization of borided pure tungsten, Surf. Coat. Technol. 194 (2) (2005) 330–334.
[26] M. Frotscher, et al., M2B5 or M2B4? A reinvestigation of the Mo/B and W/B system, Zeitsch. Anorg. Allgem. Chem. 633 (15) (2007) 2626–2630.
[27] T. Lundström, The structure of Ru2B3 and WB2. 0 as determined by single-crystal diffractometry, and some notes on the WB system, Arkiv Kemi 30 (1968) 115.
[28] P.A. Romans, M.P. Krug, Composition and crystallographic data for the highest boride of tungsten, Acta Crystallogr. 20 (2) (1966) 313–315.
[29] Kayhan, M., Transition metal borides: synthesis, characterization and superconducting properties. 2013.
[30] G. Kresse, J. Hafner, Ab initio molecular dynamics for liquid metals, Phys. Rev. B 47 (1) (1993) 558–561.
[31] G. Kresse, J. Hafner, Ab initio molecular-dynamics simulation of the liquid-metal–amorphous-semiconductor transition in germanium, Phys. Rev. B 49 (20) (1994) 14251–14269.
[32] G. Kresse, J. Furthmüller, Efficiency of ab-initio total energy calculations for metals and semiconductors using a plane-wave basis set, Comput. Mater. Sci. 6 (1) (1996) 15–50.
[33] J.P. Perdew, K. Burke, M. Ernzerhof, Generalized gradient approximation made simple, Phys. Rev. Lett. 77 (18) (1996) 3865–3868.
[34] P.E. Blöchl, Projector augmented-wave method, Phys. Rev. B 50 (24) (1994) 17953–17979.
[35] G. Kresse, D. Joubert, From ultrasoft pseudopotentials to the projector augmented-wave method, Phys. Rev. B 59 (3) (1999) 1758–1775.
[36] H.J. Monkhorst, J.D. Pack, Special points for Brillouin-zone integrations, Phys. Rev. B 13 (12) (1976) 5188–5192.
[37] M. Methfessel, A.T. Paxton, High-precision sampling for Brillouin-zone integration in metals, Phys. Rev. B 40 (6) (1989) 3616–3621.
[38] S.S. Setayandeh, et al., A DFT study to determine the structure and composition of ε-W2B5−x, J. Alloys Compd. 911 (2022), 164962.
[39] S.L. Dudarev, et al., Electron-energy-loss spectra and the structural stability of nickel oxide: An LSDA+U study, Phys. Rev. B 57 (3) (1998) 1505–1509.
[40] R. Grau-Crespo, et al., Symmetry-adapted configurational modelling of fractional site occupancy in solids, J. Phys. Condens. Matter 19 (25) (2007), 256201.
[41] K.-D. Liss, et al., Echidna—the new high-resolution powder diffractometer being built at OPAL, Physica B 385-386 (2006) 1010–1012.
[42] M. Avdeev, J.R. Hester, ECHIDNA: a decade of high-resolution neutron powder diffraction at OPAL, J. Appl. Crystallogr. 51 (6) (2018) 1597–1604.
[43] D.R. Black, et al., Certification of standard reference material 660B, Powder Diffr. 26 (2) (2011) 155–158.
[44] B.H. Toby, R.B. Von Dreele, GSAS-II: the genesis of a modern open-source all purpose crystallography software package, J. Appl. Crystallogr. 46 (2) (2013) 544–549.
[45] V.F. Sears, Neutron scattering lengths and cross sections, Neutron News 3 (3) (1992) 26–37.
[46] Neutron activation and scattering calculator [Accessed 31 June 2022]. Available from: https://www.ncnr.nist.gov/resources/activation/.
[47] N.N. Zhuravlev, The X-ray structural analysis of SiB_6, Kristallografiya 1 (1956) 666–668.
[48] H. d'Amour, W. Denner, H. Schulz, Structure determination of α-quartz up to 68 x 108 Pa, Acta Crystallogr. Sect. B: Struct. Crystallogr. Cryst. Chem. 35 (3) (1979) 550–555.
[49] Kiessling, R., et al., The crystal structures of molybdenum and tungsten borides. 1947. 1: p. 893-916.
[50] Q. Li, et al., Global structural optimization of tungsten borides, Phys. Rev. Lett. 110 (13) (2013), 136403.
[51] C. Zhao, et al., Unexpected stable phases of tungsten borides, Phys. Chem. Chem. Phys. 20 (38) (2018) 24665–24670.
[52] C. Gu, et al., Crystal structures and formation mechanisms of boron-rich tungsten borides, Phys. Rev. B 104 (1) (2021), 014110.
[53] X.Y. Cheng, et al., Computational materials discovery: the case of the W-B system, Acta Crystallogr. C Struct. Chem. 70 (Pt 2) (2014) 85–103.
[54] E.A. Brandes, G. Brook, Smithells Metals Reference Book, eighth edition, Elsevier, 2013, pp. 11–113.